First-principles calculations of phonons and Raman spectra in monoclinic $CsSnCl_3$

Ling-yi Huang and Walter R. L. Lambrecht
Department of Physics, Case Western Reserve University, Cleveland, Ohio 44106-7079, USA
(Received 30 December 2014; published 20 February 2015)

Density functional perturbation theory is used to calculate the phonons at the zone center for monoclinic $CsSnCl_3$. We report the calculated normal mode frequencies classified according to irreducible representations for both infrared-active and Raman-active modes. We also report the dielectric constants and Born-effective charges and investigate the anisotropy of the nonanalyticities near the zone center. The first-principles calculated Raman-active phonon frequencies and simulated Raman spectra are compared with experimental results from literature. We find that aside from the first-order allowed Raman modes of A_g and B_g symmetries, forbidden LO Raman modes appear prominently in the measured spectra. Several of these modes are close to or coincide with allowed modes and alter their intensity, while others appear as separate otherwise unexplained peaks. With this interpretation, good agreement is obtained with experimental mode frequencies to within a few cm^{-1}.

DOI: 10.1103/PhysRevB.91.075206 PACS number(s): 63.20.dk, 78.30.Hv

I. INTRODUCTION

Halide perovskites ABX_3, where B can be Sn or Pb, X can be I, Br, or Cl, and A can be Cs, CH_3NH_3 (methylammonium, MA), or $HC(NH_2)_2$ (formamidinium, FA) have recently attracted considerable attention as solar cell materials [1–14]. Recently, about 16% energy conversion efficiencies have been achieved by using these materials in different solar cell designs [4,8,10,15]. Although high conversion efficiencies have been realized, the underlying reasons for this success and the stability of the materials are not yet fully understood.

In two recent papers [16,17], we performed electronic and phonon band-structure calculations for different phases of $CsSnX_3$, where $X =$ I, Br, and Cl. We pointed out several interesting properties of these materials, for example, their unusual "orbital-inverted" band structure, anomalous temperature dependence of the gap, high-hole mobility, large static dielectric constant, the appearance of the LO phonon in IR absorption spectrum, a strong LO-plasmon coupling effect, etc. We also studied the relationship between some of the observed phase transitions and soft phonons. This study focused on the well-known octahedral rotations. However, aside from the perovskite structure, which has only corner-sharing octahedra, some of these materials also possess structures in which octahedra share edges. We already showed [16] that the so-called yellow phase in $CsSnI_3$ and the monoclinic $CsSnCl_3$ phases have very different band structures, with higher band gaps, and are hence less suitable for solar cell applications. Nonetheless, a better understanding of the lattice dynamics of these phases and their relation to the perovskite structure is important for the stability of the latter.

In this paper, we present a study of the zone-center phonons for monoclinic M-$CsSnCl_3$. Extensive experimental data are available in literature on the Raman spectra in this material but they have not been compared in detail with first-principles calculations.

While $CsSnCl_3$ in the perovskite structure is less suitable for solar cells because of its higher band gap than the $CsSnI_3$, it is still of interest as the end member of mixed $CsSn(I_{1-x}Cl_x)_3$ and addition of Cl has been found to increase solar cell efficiencies [5]. The reasons for this are presently not clear although they have been speculated to be due to improved crystal growth. The other reason this material is interesting is that below 390 K it undergoes a phase transition to a monoclinic structure with even larger band gap, which differs from the yellow phase occurring for $CsSnI_3$. Understanding the various possible phase transitions and structures in the trihalides is important for the long-term stability of these materials in solar cells.

II. COMPUTATIONAL METHOD

To calculate zone-center phonon frequencies and simulated infrared (IR) and Raman spectra, we use the density functional perturbation theory (DFPT) [18,19] within the local density approximation (LDA). The ABINIT code [20] with norm-conserving pseudo-potentials [21] was used for these calculations. We first fully relaxed the crystal structures with respect to the lattice constants and internal parameters. Then, after iterative minimization of the ground-state total energy, the first-order perturbation of the wave functions with respect to atomic displacements and static electric fields is performed. In practice, the second-order derivatives of the total energy with respect to atomic displacements gives us the force constants or dynamical matrix, while the second-order derivatives of the total energy with respect to the static electric fields allow us to obtain the high-frequency dielectric tensor. The Born-effective charges are obtained by the derivatives of the total energy with respect to both atomic displacements and static electric fields. The above linear-response calculations not only allow us to obtain the nonanalytic LO-TO splitting at Γ, we can also extract the matrix elements for the infrared spectra once eigenvectors and oscillator strength are obtained. In order to simulate Raman spectra, we need to know the Raman tensors which can be obtained by the third derivatives of the total energy with respect to an atomic displacement and twice with respect to the electric fields. We determined that a $3 \times 9 \times 6$ **k**-point grid and a plane-wave cutoff energy of 50 hartrees are sufficiently converged.

III. RESULTS

A. Lattice parameters

We start the (crystal) structural relaxation from the experimental crystal structure by Poulsen *et al.* [22] which showed

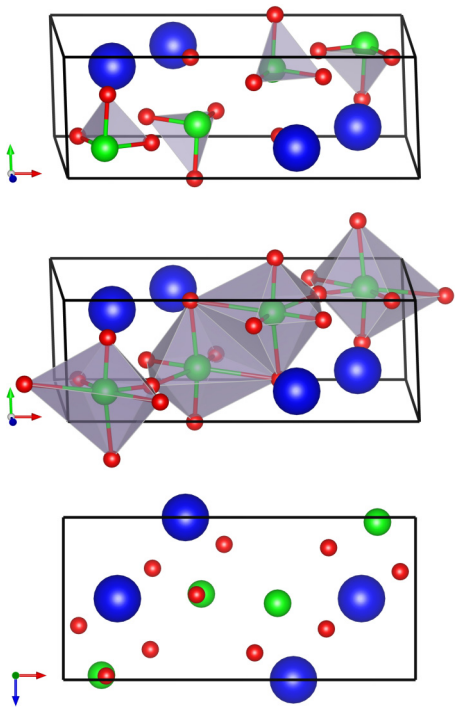

FIG. 1. (Color online) Crystal structure of M-$CsSnCl_3$ in a unit cell. The large blue spheres are Cs atoms, the intermediate size green ones are Sn atoms, and the small red ones are Cl atoms. The red horizontal arrow is in the a_1 direction, the green one (vertical in top two figures, and out of page in bottom one) is in the a_2 direction, and the blue one (out of page in top two and vertical down in bottom one) is in the a_3 direction. The top figure shows only the shortest Sn-Cl bonds highlighting the Sn-Cl tetrahedral units, while the lower figure includes the longer Sn-Cl bonds so as to show the distorted octahedral environment, indicating edge-sharing octahedra.The bottom picture is a projection along a_2.

that the space group of the M-$CsSnCl_3$ is $P2_1/c$ or C_{2h}^5 or No. 14 according to the International Tables for Crystallography. The crystal structure is shown in Fig. 1. The lattice constants are $a = 16.10$ Å, $b = 5.748$ Å, $c = 7.425$ Å, with the angle γ between a_1 and a_2 93.2°, where a_1, a_2, and a_3 are primitive unit vectors in real space and we choose a_1 to coincide with the x axis and a_3 with the z axis. Our calculated lattice parameters (with experimental ones) are listed in Table I. We note that LDA underestimates the lattice constants, respectively, by 4.5%, 3.8%, and 3.9% and the volume $V = abc \sin\gamma$ by 11.8%. Please note that this choice has the $a_2 = b$ and $a_3 = c$ lattice vectors interchanged from Ref. [22] to make the z axis coincide with the twofold symmetry axis. Atomic positions are listed in Table II.

TABLE I. Lattice parameters of M-$CsSnCl_3$.

	a (Å)	b (Å)	c (Å)	γ (°)
Expt. [22]	16.10	5.748	7.425	93.2
Calc.	15.37	5.529	7.132	93.12

B. Group theory analysis and internal coordinates.

The space group of M-$CsSnCl_3$ is C_{2h}^5 or $P2_1/c$ and the point group is C_{2h} or $2/m$. In relation to the International Tables of Crystallography, we choose the unit cell choice with unique axis c and cell choice 2, labeled $P112_1/n$. The twofold symmetry axis is along the z axis and is a screw axis placed at $\frac{1}{4}$ along the a_1 and a_2 axes, the mirror plane is a diagonal (n-type) glide mirror placed at $\frac{1}{4}$ along the a_3 axis. The inversion center occurs at the origin. One may easily recognize these symmetry operations in Fig. 1. Numbering the Cs atoms and the $SnCl_3$ units from left to right, as 1-4, the twofold rotations relate, for example, 1 to 2, the glide plane relates 1 to 3, and the inversion 1 to 4.

There are 20 atoms in the unit cell ($Z = 4$) and thus 60 displacement degrees of freedom. Each element occupies a $4e$ Wyckoff position, meaning, for example, that there are three distinct Cl atoms in the structure. Therefore, it is sufficient to consider the decomposition in irreducible representations for one Wyckoff $4e$ site. The displacements of these four atoms build a 12×12 reducible representation which is easily seen to decompose in three irreducible ones of each irreducible representation, because only the identity maps the atom into itself. Thus, in total $15A_g + 15B_g + 15A_u + 15B_u$ at the zone center are predicted. Among those modes, three modes, $A_u + 2B_u$, are acoustic modes (pure translation of

TABLE II. Summary of group theory analysis for M-$CsSnCl_3$. The atomic coordinates in parentheses are from experimental data by Poulsen *et al.* [22], the other ones are obtained by structural relaxation in this work.

Phase	Element	Wyckoff position	Reduced coordinates x	y	z	Irreducible representation	Total modes
M-$CsSnCl_3$	Cs	$4e$	0.1559 (0.1534)	0.7394 (0.7504)	0.5103 (0.5002)	$3A_g + 3B_g + 3A_u + 3B_u$	12
(C_{2h}^5, C_{2h})	Sn	$4e$	0.3928 (0.3917)	0.2652 (0.2610)	0.4810 (0.4713)	$3A_g + 3B_g + 3A_u + 3B_u$	12
	Cl(1)	$4e$	0.2478 (0.2532)	0.2547 (0.2705)	0.3066 (0.3134)	$3A_g + 3B_g + 3A_u + 3B_u$	12
	Cl(2)	$4e$	0.4578 (0.4565)	0.2783 (0.2673)	0.1598 (0.1660)	$3A_g + 3B_g + 3A_u + 3B_u$	12
	Cl(3)	$4e$	0.3814 (0.3784)	0.7834 (0.8165)	0.4815 (0.4763)	$3A_g + 3B_g + 3A_u + 3B_u$	12
		20 atoms/unit cell ($Z = 4$)				$15A_g + 15B_g + 15A_u + 15B_u$	60
	Γ_{silent}	= no silent mode					
	Γ_{acoustic}	$= A_u + 2B_u$					
	Γ_{IR}	$= 14A_u + 13B_u$					
	Γ_{Raman}	$= 15A_g + 15B_g$					

TABLE III. The static dielectric constant ε_0 and the high-frequency dielectric constant ε_∞ and generalized Lyddane-Sachs-Teller relation in M-$CsSnCl_3$.

	ε_∞	ε_0	$\frac{\varepsilon_0}{\varepsilon_\infty}$	$\prod_i(\frac{\omega_{Li}}{\omega_{Ti}})^2$
ε_{xx}	3.92	9.86	2.51	2.51
ε_{yy}	5.84	37.9	6.50	6.50
ε_{xy}	−0.105	−3.80		
ε_{zz}	3.63	7.66	2.11	2.11

all atoms) with zero frequencies because A_u corresponds to a vector along z and any vector in the xy plane corresponds to B_u irreducible representation. For the same reason, there are 27 infrared-active modes, $14A_u + 13B_u$. A mode with A_u symmetry can produce a long-range electric field in the z direction which will affect the frequency in the $\mathbf{q} \to 0$ limit for $\mathbf{q} \parallel z \parallel a_3$. In other words, by including an electric field in the z or a_3 direction, we obtain the A_u^{LO} modes. For any electric field in the xy plane, the B_u modes will behave nonanalytically for $\mathbf{q} \to 0$ but the result will depend on which direction we choose in the xy plane. In practice, we choose an electric field x along a_1 or along $y \perp x$ which is close to the a_2 axis. We label these as $B_u(x)^{LO}$ or $B_u(y)^{LO}$. The remaining 30 modes, $15A_g + 15B_g$, are Raman-active modes. No silent modes exist in this case. We summarize the results from the group theory analysis as well as our calculated and the experimental internal coordinates of the atoms in Table II. The internal parameters together with the lattice parameters determine the bond lengths. Experimentally, the bond lengths of Sn-Cl in a pyramid are 2.50, 2.52, and 2.55 Å, respectively [22]. However, in our relaxed crystal structure, the bond lengths of Sn-Cl in a pyramid are 2.50, 2.55, and 2.66 Å, and are thus slightly overestimated for the longer bonds, which is a little surprising because LDA tends to do the opposite.

C. Infrared modes

In this section, we focus on the infrared modes. The latter exhibit LO-TO splittings at the zone center which are closely related to the dielectric constant and the Born-effective charges. In Table III, we list the calculated static dielectric constant tensor elements $\varepsilon^0_{\alpha\beta}$ and the high-frequency dielectric constant $\varepsilon^\infty_{\alpha\beta}$ and check the generalized Lyddane-Sachs-Teller relation [23]

$$\prod_i \left(\frac{\omega_{Li\alpha}}{\omega_{Ti}}\right)^2 = \frac{\varepsilon^0_{\alpha\alpha}}{\varepsilon^\infty_{\alpha\alpha}} \quad (1)$$

for M-$CsSnCl_3$ Here, the product is over all modes belonging to the irreducible representation of the direction α. Note that the LO mode depends on the chosen direction α. For $\alpha = z$ this means A_u, for x or y it means B_u modes, but the results still depend on the choice x or y. Because the system is monoclinic, we note that there is also a nonzero xy element of the dielectric tensor. Similarly, the Born-effective charges have nonzero xy elements although we find these to be very small because the angle γ is close to 90°. The Born-effective charges are listed in Table IV. We can see that they substantially differ from the nominal valence of the elements, which are +1 for Cs, +2 for Sn, and −1 for Cl. The yy component of Sn is much higher

TABLE IV. Effective charges of compound elements in different directions in M-$CsSnCl_3$.

	Cs	Sn	Cl(1)	Cl(2)	Cl(3)
xx	1.33	2.82	−1.93	−1.16	−1.06
yy	1.48	4.41	−0.777	−0.594	−4.52
xy	−0.0246	−0.138	−0.0210	−0.0265	0.210
zz	1.35	2.51	−1.29	−1.88	−0.686

than the x and y components, meaning that the Sn atoms feel stronger long-range electrostatic forces in the y direction. The same is true for the Cl(3) atoms.

Our calculated infrared-active phonon frequencies and the corresponding oscillator strengths are listed in Table V and the simulated IR spectra are shown in Fig. 2, from top to bottom, for B_u(x), B_u(y), and A_u modes, respectively.

As in the case of cubic phase $CsSnBr_3$ and $CsSnCl_3$ [17], the LO phonons which are most strikingly seen in the loss spectrum $-\mathrm{Im}\,\varepsilon(\omega)^{-1}$ also produce notable peaks in the IR absorption spectra because of the corresponding minima in the index of refraction and $\mathrm{Re}\,\varepsilon(\omega)$.

Examining the infrared-active modes, we can see that the lower-frequency modes have low oscillator strength and correspondingly small LO-TO splittings. This is expected because they are in modes in which the Cs ions move together with the $SnCl_3$ units but show no well-defined ionic bond stretches. On the other hand, several modes tend to have a dominant oscillator strength either in the x or y direction, which is not surprising because the monoclinic angle is close to 90°. In the spectrum corresponding to $B_u(x)$ we can see six peaks in $\mathrm{Im}\,\varepsilon(\omega)$ with corresponding peaks increasingly split away by LO-TO splitting in the $-\mathrm{Im}\,\varepsilon^{-1}(\omega)$. They correspond to modes 1, 2, 5, (6,7), (8,9), 12, where groups put together in parentheses form one peak because of their closeness in frequency. The highest LO-TO splitting for nonanalyticity in the x direction, i.e., modes that interact with a long-range electric field in the x direction produced by dipoles in the x direction, occurs for mode B_u^{12}. Its LO-TO splitting is $(247 - 202) = 45\ \mathrm{cm}^{-1}$.

The spectrum for $B_u(y)$ looks quite different. Here, we see only four peaks in $\mathrm{Im}\,\varepsilon(\omega)$ corresponding to modes 2, 5, (6,7), 10. We can see that these are the modes with highest S_{yy}. It is interesting to note that B_u^{12} has a small oscillator strength S_{yy} but nevertheless a large LO-TO splitting. This suggests that the LO-y mode most closely corresponding to B_u^{12} instead is $B_u^{11}(\mathrm{LO}y)$. Similarly, we can shift the modes $B_u^{7\text{-}10}(\mathrm{LO}y)$ to $B_u^{8\text{-}11}(\mathrm{LO}y)$. In fact, mode 6 has the highest oscillator strength S_{yy} and is thus expected to have the largest LO-TO splitting. To test, this idea we show in Fig. 3 the displacement pattern of mode $B_u^6(\mathrm{TO})$ compared to the mode $B_u^{12}(\mathrm{LO}y)$. One can clearly see that the y projection of mode $B_u^6(\mathrm{TO})$ matches well with that of $B_u^{12}(\mathrm{LO}y)$. Both show an internal vibrational mode of the $SnCl_3$ pyramid in the y direction, which is in antiphase between groups related by inversion symmetry, say groups 2-3 and 1-4 counting them from left to right. On the other hand, the $B_u^6(\mathrm{TO})$ has a diagonal motion with also an x component. Apparently, the y component of this mode strongly couples to the electric field in the y direction which leads to the very strong $(229 - 93) = 136\ \mathrm{cm}^{-1}$ LO-TO splitting. One

TABLE V. Infrared-active phonon modes of M-$CsSnCl_3$. All frequencies are in units of cm^{-1}.

		LO modes			Oscillator strengths (in a.u.)			
Mode	TO	$B_u^{LO}(x)$	$B_u^{LO}(y)$	$A_u^{LO}(z)$	S_{xx}	S_{yy}	S_{xy}	S_{zz}
A_u^1	33			33				1.3×10^{-7}
A_u^2	43			43				3.3×10^{-7}
A_u^3	50			51				4.9×10^{-6}
A_u^4	56			61				2.5×10^{-5}
A_u^5	68			70				7.2×10^{-6}
A_u^6	82			82				1.7×10^{-6}
A_u^7	88			88				2.8×10^{-6}
A_u^8	95			96				1.2×10^{-5}
A_u^9	102			103				1.1×10^{-5}
A_u^{10}	111			112				9.4×10^{-6}
A_u^{11}	123			127				3.3×10^{-5}
A_u^{12}	145			151				5.3×10^{-5}
A_u^{13}	212			220				1.3×10^{-4}
A_u^{14}	254			281				2.6×10^{-4}
B_u^1	31	33	31		5.3×10^{-6}	1.8×10^{-7}	-9.6×10^{-7}	
B_u^2	56	58	57		1.2×10^{-5}	3.8×10^{-5}	-2.1×10^{-5}	
B_u^3	60	60	60		2.5×10^{-7}	2.4×10^{-6}	-7.7×10^{-7}	
B_u^4	77	77	77		4.9×10^{-6}	2.0×10^{-7}	9.9×10^{-7}	
B_u^5	79	84	82		5.2×10^{-5}	3.4×10^{-4}	-1.3×10^{-4}	
B_u^6	93	94	95		1.4×10^{-5}	8.9×10^{-4}	1.1×10^{-4}	
B_u^7	96	98	109		1.5×10^{-5}	4.1×10^{-4}	-7.9×10^{-5}	
B_u^8	109	113	114		6.3×10^{-5}	1.4×10^{-7}	3.0×10^{-6}	
B_u^9	115	121	124		1.6×10^{-5}	1.4×10^{-5}	-1.5×10^{-5}	
B_u^{10}	125	126	157		3.0×10^{-6}	2.7×10^{-5}	-9.1×10^{-6}	
B_u^{11}	157	157	201		6.9×10^{-6}	1.4×10^{-9}	-9.9×10^{-8}	
B_u^{12}	202	247	229		4.6×10^{-4}	5.2×10^{-6}	4.9×10^{-5}	
B_u^{13}	261	261	261		3.9×10^{-7}	2.3×10^{-6}	9.5×10^{-7}	

may also note that the groups (2-3) and (1-4) which are in antiphase with each other in their motion are displaced in the y direction from each other and correspond to edge-sharing octahedra in the structure as seen in Fig. 1(b). Of course, strictly speaking all $B_u(\mathrm{LO}y)$ modes together result from interactions of the electric field with all $B_u(\mathrm{TO})$ modes together and, thus, the only unambiguous way of counting them is from lower to higher frequency as listed in Table V. Still, the crossing of modes suggested above explains in a natural way the broad reststrahlen band between about 100 and 200 cm^{-1} seen in the predicted IR reflectivity for electric field in the y direction. For the A_u modes, we see a spectrum of more or less evenly separated peaks in Im $\varepsilon(\omega)$ with increasingly larger LO-TO splittings with increasing frequency. Unfortunately, no experimental data have been reported to the best of our knowledge on the infrared spectra.

To conclude this section on infrared spectra, we show in Fig. 4(a) the predicted angular dependence in the xy plane of the B_u^{LO} modes. The angle $\theta = 0$ corresponds to the x axis. This also very strongly suggests a crossing of the modes 10 and 11 near 45°. Strictly speaking, we cannot have crossings of modes of the same symmetry and thus we really see an avoided crossing. This picture suggests a different relation between modes than the one discussed earlier purely based on the LO splitting with nonanalyticity in the y direction, where we identified the mode pattern of the $B_u^{12}(\mathrm{LO}y)$ with the y motion of the $B_u^6(\mathrm{TO})$. From the full angular dependence it rather appears that mode 11 only crosses 10 and possibly 9. Again, one cannot strictly speaking associate individual TO to LO modes but should consider the whole LO spectrum with a given nonanalyticity because the LO spectrum with each type of nonanalyticity, i.e., direction of the electric field in the plane results from the diagonalization of a different dynamical matrix with different long-range forces.

We also show the angular dependence of the static and high-frequency dielectric constants in Fig. 4(b). Diagonalizing the static dielectric tensor one obtains as principal values $\varepsilon_1^0 = 38.41$, $\varepsilon_2^0 = 9.35$ with the long principal axis at 97° and the short principal axis at 187°. The long principal axis is close to the a_2 crystallographic direction, but not quite. For ε^∞, the principal axes are at 93° and 183°, so closer to the crystal axes and the principal values are 5.845 and 3.914 very close to the yy and xx values because the xy value is quite small.

D. Raman modes and comparison with experiment

Our calculated Raman-active phonon frequencies are shown in columns 4 and 5 of Table VI together with their symmetry assignment based on the corresponding eigenvectors and Raman tensors. The corresponding experimental assignments in columns 1–3 will be discussed in the following. The last two columns show LO modes which, as we will argue, occur in the spectra as forbidden LO modes through the Fröhlich scattering mechanism [24–26] The simulated Raman spectra for specific Raman tensor components are shown in Fig. 5.

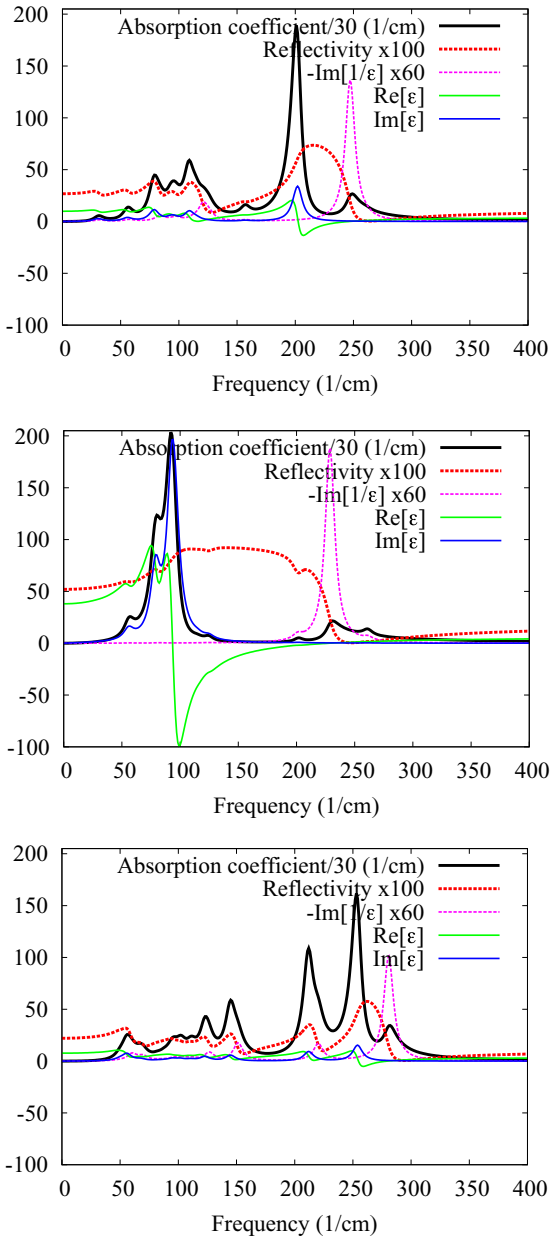

FIG. 2. (Color online) Figures, from top to bottom, show the real and imaginary parts of dielectric function ε, imaginary part of $-1/\varepsilon$, absorption coefficient and reflectivity of $B_u(x)$, $B_u(y)$, and A_u modes, respectively, in M-$CsSnCl_3$.

We found three papers showing the Raman spectra for M-$CsSnCl_3$. They actually are from the same research group, Kuok's group in the National University of Singapore. The first paper [27], published in 1987, shows the Raman spectra from room temperature to 85 K and concludes that no phase transition occurs within that temperature range. The second paper [28], published in 1992, shows the polarized Raman spectra from 10 to 423 K, which provides evidence of a phase transition in $CsSnCl_3$ to the cubic perovskite phase at about 385 K. The third paper [29], published in 1994, studies additional phase transitions of $CsSnCl_3$ under high pressure. Although we do not address the phase transition under a high-pressure situation in this paper, their Raman spectra at

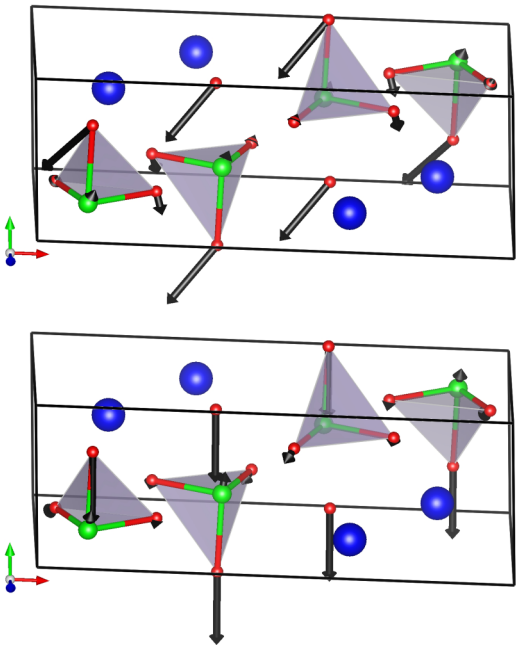

FIG. 3. (Color online) Upper figure shows the displacement patters of B_u^6(TO) mode, at 93 cm^{-1}, without nonanalyticity. The lower figure shows the displacement pattern of the mode at 229 cm^{-1} when the nonanalyticity is in the y direction. The large blue spheres are Cs atoms, the medium green ones are Sn atoms, and the small red ones are Cl atoms. The red arrow is in the a_1 direction, the green one is in the a_2 direction, and the blue one is in the a_3 direction.

0 kbar show the latest experimental Raman spectra we could find for M-$CsSnCl_3$.

Although these papers list various Raman frequencies in their discussion, the authors did not clearly label the frequencies of the peaks in their Raman spectra shown in their papers. In order to more accurately compare our calculated results with the experimental spectra, we first need to know the frequencies of all obvious peaks in the experimental spectra. To this end, we digitalize their experimental Raman spectra shown in these three papers. Figure 6 shows the digitalized results. The first (top) spectrum, labeled by 1, is digitalized from the spectrum recorded at 85 K in Fig. 2 in the first paper [27]. The second spectrum, labeled by 2, is digitalized from polarized (zz) Raman spectrum at 10 K in the Fig. 1 in the second paper [28]. And, the remaining spectra, labeled by 3 to 5, are from three spectra in the Fig. 1 in their third paper [29]. Digitalization, of course, contains some errors; for example, it looks like the frequency of the first peak in the spectrum 2 (25.3 cm^{-1}) is lower than the frequency of the first peak (23.8 cm^{-1}) in the spectrum 4. However, our purpose here is not to determine more precise mode frequencies from the experimental Raman spectra, rather we wish to associate the modes as identified in the papers with specific peaks in the spectrum so we can also discuss the corresponding intensities.

Unfortunately, the three experimental papers do not fully describe the scattering geometry. The authors specify that the crystals are needlelike and with the needle axis coinciding with their choice of c axis, which is our b axis. The mentioned (zz) polarization should then correspond to our $\mathbf{E} \parallel b$ or our (yy) polarization. In the most recent paper, they only state

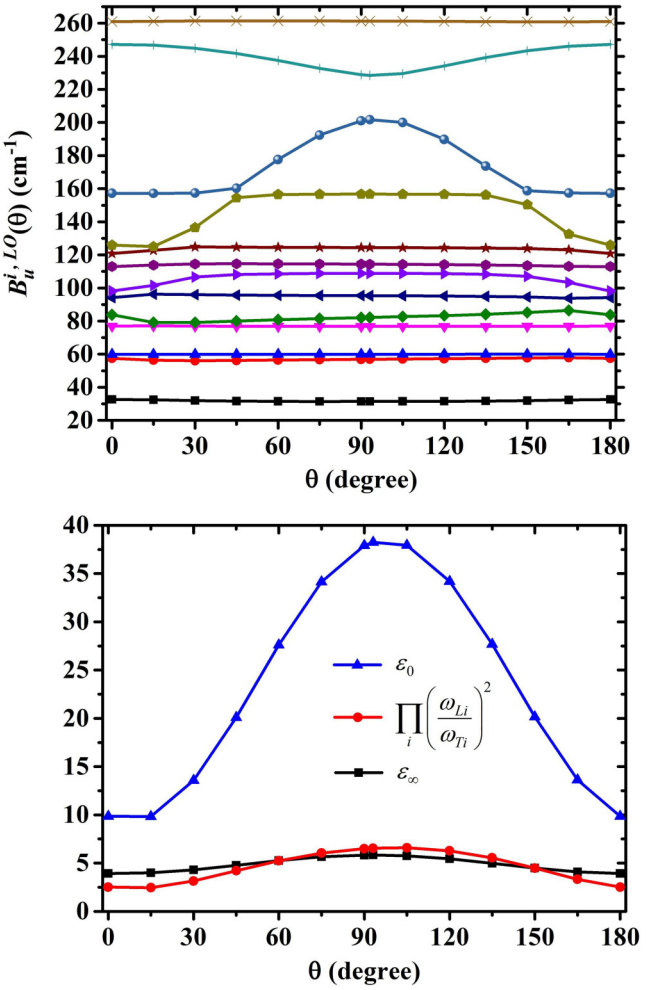

FIG. 4. (Color online) Upper figure shows the angular dependence of each B_u^i(LO) mode, where $i = 1$ to 13 from low to high frequency. The abscissa θ is the azimuthal angle measured from the x axis. The lower figure shows the angular dependence of the static dielectric constant ε_0, the high-frequency dielectric constant ε_∞, and $\prod_i(\frac{\omega_{Li}}{\omega_{Ti}})^2$.

the crystal is mounted vertical or horizontal and the beam is perpendicular to or parallel to the crystal axis. This, however, does not tell us the actual polarization.

In Table VI we list the thus determined experimental peak positions as well as explicitly quoted frequencies in the papers from lower to higher frequency which allows us to see the correspondence with calculated modes based purely on frequency value. We also give the symmetry assignment made in the experimental papers. Generally speaking, we find a good one-to-one match and agreement to within a few cm^{-1} for the low-frequency modes up to about 95 cm^{-1} although our assignments as A_g or B_g do not always agree with the experimental papers. For the higher-frequency modes, the discrepancies are higher and the assignments are less clear, so we discuss them later.

Kuok's [27] analysis of the spectra is based on separating internal vibration modes of the $SnCl_3$ units at higher frequencies from crystal translational and/or molecule librational modes. The internal motions of the $SnCl_3^-$ radical, which has C_{3v} symmetry, were reported by Woodward and Taylor [30] but

TABLE VI. Raman-active modes. First column: experimental peak position from digitized data from Kuok *et al.* [27–29]; second column: type of mode [27], librational (l), translational (t), or ν_n, $n =$ 1–4, internal modes of $SnCl_3^-$; third column: symmetry assignment from Ref. [28]; fourth column: our calculated Raman-active modes; fifth column: our symmetry assignment; seventh column: A_u^{LO} modes; eighth column: B_u^{LO} modes giving either range or for specifically x or y direction. Forbidden LO modes may occur through the Fröhlich mechanism.

Raman	Type	Sym [28]	Calc.	Sym	A_u^{LO}	B_u^{LO}
12-17	t	B_g	11	B_g^1		
23-26	l	A_g	27	A_g^1		
33-35	l	A_g	33	A_g^2	33	31-33
38-40	t		38	B_g^2		
41		A_g	43	A_g^3	43	
42	t	B_g	44	B_g^3		
48-49	t	A_g	46	A_g^4		
52-53	t	B_g	53	B_g^4	51	
55-56	l	A_g	57	A_g^5		57-58
61	t		62	B_g^5	61	60
68		B_g			70	
71-72	t	B_g	73	B_g^6		
76			75	A_g^6		77
79		A_g	79	B_g^7		
81-82	ν_4	A_g	82	A_g^7	82	82-84
88			86	A_g^8	88	
93		B_g	92	B_g^8		
95	ν_4	A_g	94	A_g^9		94-95
			96	B_g^9	96	
			103	A_g^{10}	103	
			104	B_g^{10}		
			106	A_g^{11}		
112-114	ν_4	A_g			112	113-114
117	ν_4		117	A_g^{12}		
			118	B_g^{11}		
121	ν_4	B_g				121-124
127-129	ν_2, ν_4	B_g	125	B_g^{12}	127	126
141-149	ν_2, ν_1	B_g	146	A_g^{13}	151	
162	l		159	B_g^{13}		157
193	l					201(y)
211	t		211	A_g^{14}		
227-231	ν_3	A_g			220	229(y)
			239	B_g^{14}		
249-253	ν_3	B_g				247(x)
263-266	ν_3	A_g	259	A_g^{15}		261
269	ν_3		269	B_g^{15}		
278-284	ν_3	B_g			281	
290	ν_1	A_g				
300-316	ν_1	B_g				

due to the lower symmetry and resulting distortions of the molecules and interactions between the molecules the modes split and the correspondence is not entirely obvious anymore. These are the modes designated as $\nu_{1\text{-}4}$. The ν_1 and ν_2 modes

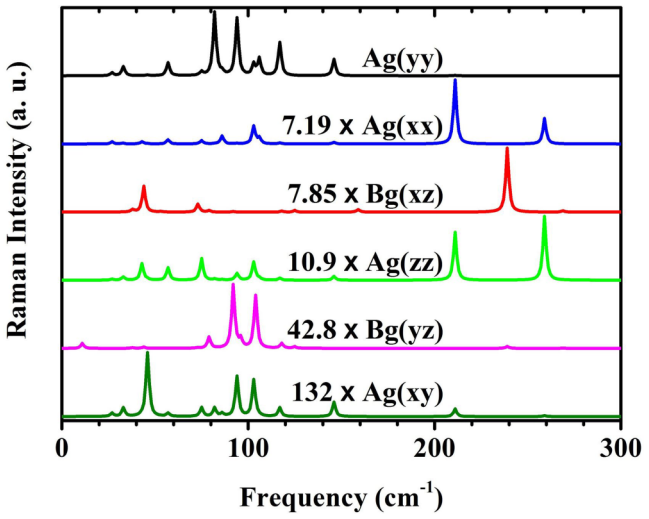

FIG. 5. (Color online) Simulated Raman spectra for M-$CsSnCl_3$. The different tensor components are scaled by different factors so as to normalize their strongest peak.

have A_1 symmetry of the C_{3v} group while ν_3 and ν_4 have doubly degenerate E symmetry of C_{3v}. In $SnCl_3^-$ radicals dissolved in ether, these occur, respectively, at 297, 128, 256, and 103 cm^{-1}. In the second paper [28], the authors based the symmetry assignment of the modes on the assumption that A_g modes are generally stronger than B_g modes. Obviously, this cannot be applied across the board.

In Kuok [27], the modes are labeled as translational or librational where this assignment was made based on the assumption that librational modes have higher intensity. As shown in Fig. 7, in the first two modes we can see the Cs and $SnCl_3$ molecules move together in, respectively, the b or the c direction for the left part of the unit cell and in the opposite direction in the right part. So, these modes look like a folded

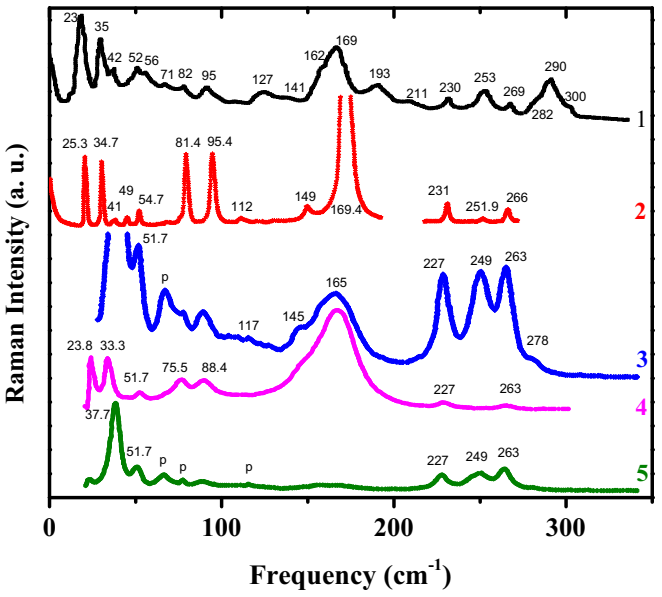

FIG. 6. (Color online) Digitalized plot of the experimental Raman spectra from Kuok *et al.* [27–29]. Note the sharpness of spectrum 2 is mostly due to the low temperature (10 K).

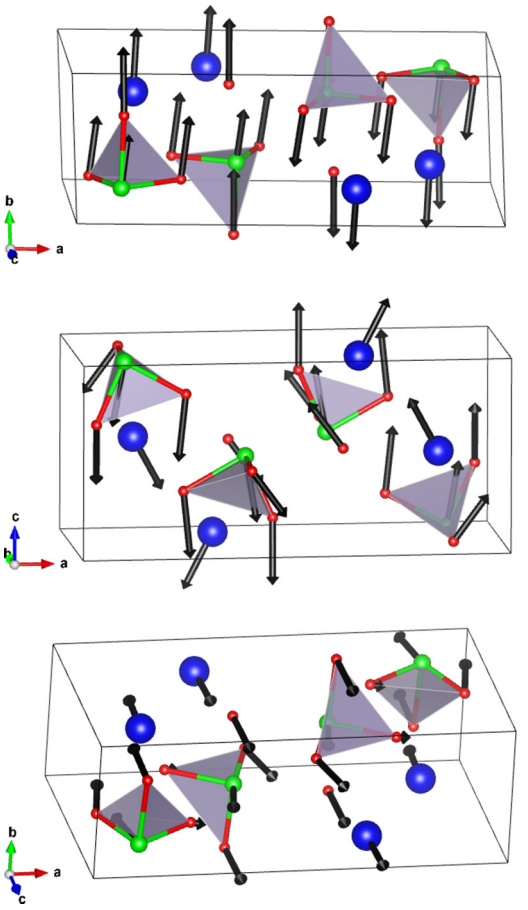

FIG. 7. (Color online) Displacement patterns for modes B_g^1, A_g^1, and A_g^2 from top to bottom. Note the different orientation of the axes.

acoustic mode and definitely have indeed mostly translational character. However, some distortion of the $CsCl_3$ molecules is visible in these modes as well. Kuok [27] identified two peaks at 23 and 26 cm^{-1} labeled as librational and translational, respectively. In his spectrum, only the 23 cm^{-1} is clearly visible and this mode is definitely more translational. We seem to overestimate this frequency somewhat. The A_g^2 mode involves a rotation about the c axis of the molecules, which could be termed librational, but also a translation of the Cs atoms relative to the molecule. The B_g^2 mode (not shown) also has mixed librational character involving the rotation of the molecules but has translations of the Cs atoms as well. The next A_g^3 mode involves a motion of Sn and two of the Cl atoms predominantly in the a direction, while the other Cl and the Cs move in the c direction. So, one could more call it translational and distortion than libration. The B_g^5 mode shows the $SnCl_3$ molecules moving relative to each other in the b direction and is indeed mostly translational. These are just a few examples; the displacement patterns of all the modes are available in the Supplemental Material [31] accompanying the paper. We conclude that some modes have indeed predominantly translational character, but many are also mixed librational and translational.

We now scrutinize this assignment further and attempt to address the higher-frequency mode discrepancies by examining the intensities. We note that the $A_g(yy)$ spectrum is

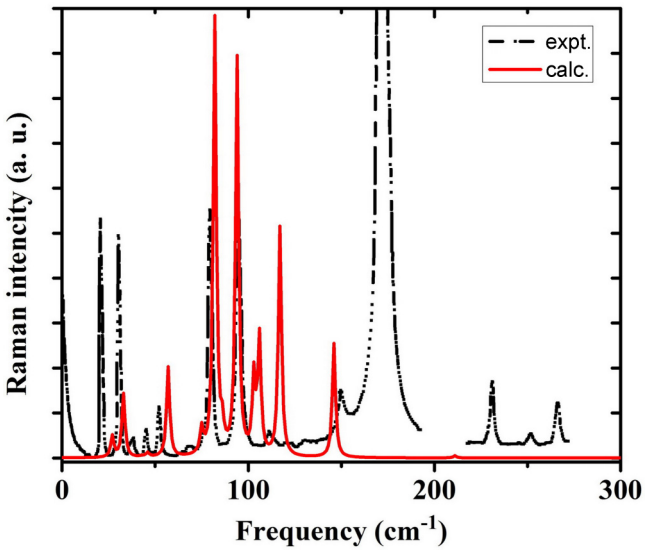

FIG. 8. (Color online) Comparison of calculated (calc.) $A_g(yy)$ spectrum with experimental (expt.) polarized Raman spectrum from Kuok [28].

clearly the strongest and can be compared most directly with Kuok's spectrum 2, which we do in Fig. 8. The strongest peaks in our calculated spectrum clearly correspond to modes A_g^7 and A_g^9 at 82 and 94 cm^{-1} which match well the peaks in the experiment at 81.4 and 95.4 cm^{-1}. The lowest-frequency modes A_g^1 and A_g^2 at 27 and 33 match the separated peaks in Kuok at 25.3 and 34.7 although these peaks are significantly smaller in our calculation compared to the experiment. As we will later argue, this is because LO modes at almost the same frequency also contribute to this mode. The A_g^3 and A_g^4 are rather weak both in our calculation and experiment but still visible in the experiment. The A_g^5 peak is stronger in our calculation than in experiment. The A_g^8 mode is relatively weak in our calculation but can be seen in spectrum 4 of Kuok *et al.* Modes $A_g^{10\text{-}12}$ are close to each other. Only the highest mode at 117 seems to match spectrum 3 and a peak at 112 in spectrum 2 but in any case our calculated peaks appear much stronger than the experiment. In spectrum 3, one can see other separate features just below it. Our mode A_g^{13} at 146 cm^{-1} matches the experimental peak at 149 cm^{-1}. The big mystery at this point is what is the enormous peak at 169 cm^{-1} present as a broad peak in all experimental spectra but not matching clearly any of our calculated A_g or B_g modes. The A_g^{14} mode at 211 cm^{-1} is only seen in spectrum 1.

In the high-frequency region, the experiment shows three clear peaks at about 230, 250, and 260 cm^{-1} in all the spectra. Our calculated A_g^{14} mode at 259 nicely matches the highest one in frequency but is very weak in intensity in our calculation compared to the experiment. Our calculated B_g^{14} mode at 239 should be strong only in xz polarization and could possibly match the 250 cm^{-1} experimental peak or the 230 cm^{-1} but none of these assignments seem to agree intensitywise. Our highest B_g^{15} at 269 cm^{-1} is predicted to be weak for any polarization.

An alternative explanation emerges when we consider the possibility of LO forbidden modes. We note that $B_u^{12}(\mathrm{LO}y)$ and $B_u^{13}(\mathrm{LO}y)$ modes at 229 and 261 cm^{-1} match very closely to the 230 and 260 experimental peaks. The 250 cm^{-1} experimental peak then matches the 247 cm^{-1} $B_u^{12}(\mathrm{LO}x)$. The $A_u^{13}(\mathrm{LO})$ mode at 220 cm^{-1} may also contribute to the experimental peak which varies between 227 and 231 and has an asymmetric shape suggesting another mode could be hidden under it at lower frequency. This seems a far more plausible explanation. Furthermore, if we now accept that LO modes appear as forbidden LO modes in the Raman spectrum through the Fröhlich mechanism, we should include all LO modes. We then notice that several low-frequency LO modes coincide almost with allowed g modes and help explain the discrepancies in intensity noticed earlier. In particular, the already strong 82 and 95 cm^{-1} modes would become even stronger, and also the 27 and 35 cm^{-1} peaks would increase in intensity.

We thus attempt to construct a separate simulated Raman spectrum for the LO modes. Unfortunately, we do not have a fully first-principles theory available for calculating the relative intensities of these modes, although based on the nature of the Fröhlich interacton [26], we may expect it to be related to the LO-TO splitting and thus choose the amplitude proportional to

$$\left(\frac{\omega_{\mathrm{LO}}^2-\omega_{\mathrm{TO}}^2}{\omega_{\mathrm{LO}}^2}\right).$$

This requires us to establish a one-to-one correspondence between LO and TO modes which we have argued is not strictly valid. For the A_u^{LO} modes, there is only one LO frequency, but for the B_u^{LO} modes, the ω_{LO} depends on the direction in the plane. For most modes, this is a small effect but as seen in Fig. 4 for mode 11 there is a big dispersion with angle. Based on this figure we assume the mode 11 crosses mode 10 and corresponds to the TO mode at 115 cm^{-1}. In that case, one might expect a peak at the average of the LOx and LOy values and a large width due to the dispersion. Using this approach, we obtain the spectrum for B_u^{LO} modes shown in Fig. 9. This simulated spectrum accounts clearly for the 165–169 cm^{-1} peak which is very strong in most polarizations but also quite broad. The peak position is close to the frequency where the crossing of modes occurs in Fig. 4. This indicates a mode with

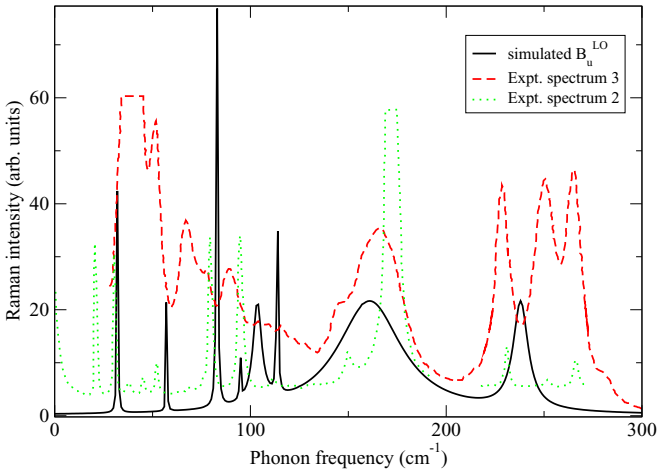

FIG. 9. (Color online) Simulated B_u^{LO} spectrum compared to experimental spectra 2 and 3.

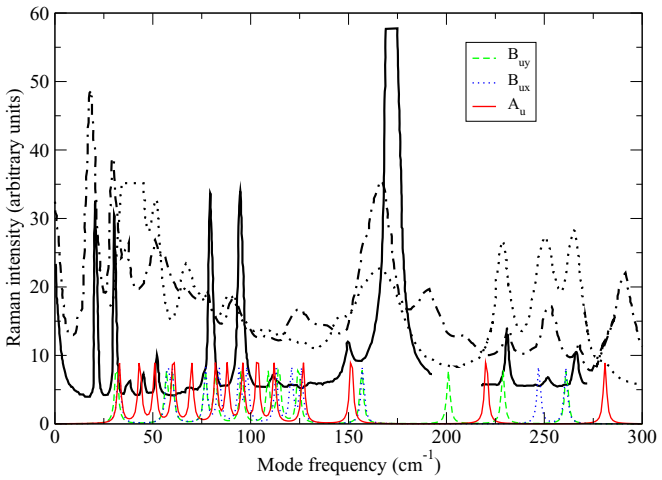

FIG. 10. (Color online) Simulated forbidden LO mode contribution to the Raman spectrum compared with experimental spectrum 1 (dashed line), 2 (solid line), and 3 (dotted line) where the numbering corresponds to Fig. 6.

large LO-TO splitting and oscillator strength for which we can also expect the strongest Fröhlich coupling mechanism. It also shows a good match for some of the other peaks at lower frequency but does not account well for the fine structure of the higher peaks above 200 cm^{-1}.

The latter appear to be more clearly related to separate LOx and LOy modes. We thus also construct a spectrum simply from the LO peak positions giving each mode equal amplitude and width and at this point do not attempt to fully account for the peak intensities. The thus constructed LO spectrum is compared with the experimental ones in Fig. 10 and shows several peaks match at least in position. Our calculations seem to slightly underestimate the peak positions corresponding to the internal vibrational modes of the $SnCl_3^-$ molecule. This may be related to our overestimate of the bond lengths noted in Sec. II.

Unfortunately, at present we do not have a fully quantitative theory for the LO forbidden peaks and some experimental features appear to correspond to LO modes for specific directions x or y while others seem to be better accounted for by an average in the xy plane. Our assignment should thus perhaps still be taken as a working hypothesis. If our assignment of some peaks as forbidden LO modes is correct, one expects these peaks to become even stronger under resonant Raman conditions, i.e., when the exciting laser frequency matches an optical absorption peak such as the near-gap free exciton. It may thus be very useful to explore this prediction in future experimental work.

In summary, then, we conclude that the measured Raman spectrum is a superposition of first-order allowed Raman modes with A_g and B_g symmetries with very prominent forbidden LO modes. This helps explain the discrepancies in intensity when directly comparing the allowed spectra alone and explains the presence of the broad and strong 169 cm^{-1} peak and explains the high 282 cm^{-1} peak.

Still there are some even higher peaks in some of the spectra at 290 and 300 cm^{-1}. These only appear in the oldest data in spectrum 1 and may be arising from different phases. In Kuok [27], the 300 cm^{-1} mode was assigned to the symmetric stretch A_1 symmetry ν_1 mode of the $SnCl_3$ molecule. However, in Kuok [29], this peak was no longer observed and instead the strong 165 cm^{-1} mode was assigned to the A_1 ν_1 because it is expected to be a strong mode. The authors already noted that this was surprising because of the large shift from the free molecule. In this paper, we propose that the very strong 165 cm^{-1} mode is instead a very strong oscillator LO forbidden mode. This may resolve this puzzle.

IV. CONCLUSIONS

In this paper, we presented a study of the zone-center phonons in monoclinic M-$CsSnCl_3$. We provided phonon frequencies and their symmetry assignment for all 60 modes. We predict the infrared absorption and reflection spectra and investigated in some detail the angular dependence of the LO modes in the xy plane. In particular, we presented evidence for mode crossing behavior. Most of all, we provide a detailed interpretation of the available Raman spectra in the literature. We show that these spectra not only contain the expected even symmetry first-order allowed Raman modes, but also prominently show forbidden LO modes. With this interpretation, our calculated phonons agree to within a few cm^{-1} with all observed peaks in Raman but our interpretation provides new symmetry assignments to several modes. We also showed that librational and translational characteristics are thoroughly mixed in several modes. Some relation to the internal modes of the $SnCl_3$ is still present as noted in earlier work. A complete set of mode displacement patterns is available in the Supplemental Material [31].

ACKNOWLEDGMENTS

This work was supported by the US Department of Energy, Office of Science, Basic Energy Sciences, under Grant No. ER-46874-SC0008933. The calculations used the High Performance Computing Resource in the Core Facility for Advanced Research Computing at Case Western Reserve University.

[1] I. Chung, B. Lee, J. He, R. P. H. Chang, and M. G. Kanatzidis, Nature (London) **485**, 486 (2012).

[2] I. Chung, J.-H. Song, J. Im, J. Androulakis, C. D. Malliakas, H. Li, A. J. Freeman, J. T. Kenney, and M. G. Kanatzidis, J. Am. Chem. Soc. **134**, 8579 (2012).

[3] H.-S. Kim, C.-R. Lee, I. Jeong-Hyeok, K.-B. Lee, T. Moehl, A. Marchioro, S.-J. Moon, R. Humphry-Baker, J.-H. Yum, J. E. Moser *et al.*, Sci. Rep. **2**, 591 (2012).

[4] J. Burschka, N. Pellet, S.-J. Moon, R. Humphry-Baker, P. Gao, M. K. Nazeeruddin, and M. Grätzel, Nature (London) **499**, 316 (2013).

[5] M. M. Lee, J. Teuscher, T. Miyasaka, T. N. Murakami, and H. J. Snaith, Science **338**, 643 (2012).

[6] J. M. Ball, M. M. Lee, A. Hey, and H. J. Snaith, Energy Environ. Sci. **6**, 1739 (2013).

[7] G. E. Eperon, V. M. Burlakov, P. Docampo, A. Goriely, and H. J. Snaith, Adv. Funct. Mater. **24**, 151 (2014).
[8] M. Liu, M. B. Johnston, and H. J. Snaith, Nature (London) **501**, 395 (2013).
[9] W. Zhang, M. Saliba, S. D. Stranks, Y. Sun, X. Shi, U. Wiesner, and H. J. Snaith, Nano. Lett. **13**, 4505 (2013).
[10] K. Wojciechowski, M. Saliba, T. Leijtens, A. Abate, and H. J. Snaith, Energy Environ. Sci. **7**, 1142 (2014).
[11] M. A. Loi and J. C. Hummelen, Nat. Mater. **12**, 1087 (2013).
[12] F. Brivio, K. T. Butler, A. Walsh, and M. van Schilfgaarde, Phys. Rev. B **89**, 155204 (2014).
[13] J. M. Frost, K. T. Butler, F. Brivio, C. H. Hendon, M. van Schilfgaarde, and A. Walsh, Nano Lett. **14**, 2584 (2014).
[14] G. E. Eperon, S. D. Stranks, C. Menelaou, M. B. Johnston, L. M. Herz, and H. J. Snaith, Energy Environ. Sci. **7**, 982 (2014).
[15] G. Hodes, Science **342**, 317 (2013).
[16] L.-y. Huang and W. R. L. Lambrecht, Phys. Rev. B **88**, 165203 (2013).
[17] L.-y. Huang and W. R. L. Lambrecht, Phys. Rev. B **90**, 195201 (2014).
[18] X. Gonze, Phys. Rev. B **55**, 10337 (1997).
[19] X. Gonze and C. Lee, Phys. Rev. B **55**, 10355 (1997).
[20] X. Gonze, J.-M. Beuken, R. Caracas, F. Detraux, M. Fuchs, G.-M. Rignanese, L. Sindic, M. Verstraete, G. Zerah, F. Jollet *et al.*, Comput. Mater. Sci. **25**, 478 (2002).
[21] C. Hartwigsen, S. Goedecker, and J. Hutter, Phys. Rev. B **58**, 3641 (1998).
[22] F. R. Poulsen and S. E. Rasmussen, Acta Chem. Scand. **24**, 150 (1970).
[23] W. Cochran and R. Cowley, J. Phys. Chem. Solids **23**, 447 (1962).
[24] R. Martin and T. Damen, Phys. Rev. Lett. **26**, 86 (1971).
[25] R. Martin, Phys. Rev. B **4**, 3676 (1971).
[26] P. Y. Yu and M. Cardona, *Fundamentals of Semiconductors Physics and Materials Properties*, 4th ed. (Springer, Heidelberg, 2010).
[27] M. H. Kuok, Phys. Status Solidi B **141**, K167 (1987).
[28] M. H. Kuok, J. Raman Spectrosc. **23**, 225 (1992).
[29] Z. X. Shen, W. L. Loo, M. H. Kuok, and S. H. Tang, J. Mol. Struct. **326**, 73 (1994).
[30] L. A. Woodward and M. J. Taylor, J. Chem. Soc. **1962**, 407 (1962).
[31] See Supplemental Material at http://link.aps.org/supplemental/10.1103/PhysRevB.91.075206 for a gzipped archive of VESTA files visualizing each of the vibrational normal modes identified by symmetry as well as a pdf file with figures of them.